New nonlinear mechanisms of midlatitude atmospheric low-frequency variability

A.E. Sterk[*,a], R. Vitolo[b], H.W. Broer[a], C. Simó[c], H.A. Dijkstra[d]

[a]*Department of Mathematics, University of Groningen, PO Box 407, 9700 AK Groningen, The Netherlands*
[b]*School of Engineering, Computing and Mathematics, University of Exeter, North Park Road, Exeter, EX4 4QF United Kingdom*
[c]*Departament de Matemàtica Aplicada i Anàlisi, Universitat de Barcelona, Gran Via 585, 08007 Barcelona, Spain*
[d]*Institute for Marine and Atmospheric Research Utrecht, Utrecht University, Princetonplein 5, 3584 CC Utrecht, The Netherlands*

Abstract

This paper studies the dynamical mechanisms potentially involved in the so-called atmospheric low-frequency variability, occurring at midlatitudes in the Northern Hemisphere. This phenomenon is characterised by recurrent non-propagating and temporally persistent flow patterns, with typical spatial and temporal scales of 6000-10000 km and 10-50 days, respectively.

We study a low-order model derived from the 2-layer shallow water equations on a β-plane channel with bottom topography, forced by a zonal wind profile and including dissipation by momentum diffusion (in both layers) and linear friction (bottom layer only). The low-order model is obtained by a Galerkin projection retaining only the Fourier modes with wavenumbers 0, 3 (zonal) and 0, 1, 2 (meridional). Orography height (h_0) and magnitude of zonal wind forcing (U_0) are used as control parameters to study the bifurcations of equilibria and periodic orbits.

A systematic analysis of the dynamics of the low-order model is performed

[*]Corresponding address: Department of Mathematics, University of Groningen, PO Box 407, 9700 AK Groningen, The Netherlands. Tel.: +31 (0)50 363 3992. Fax: +31 (0)50 363 3800.

Email addresses: a.e.sterk@rug.nl (A.E. Sterk), r.vitolo@ex.ac.uk (R. Vitolo), h.w.broer@rug.nl (H.W. Broer), carles@maia.ub.es (C. Simó), dijkstra@phys.uu.nl (H.A. Dijkstra)

using techniques and concepts from dynamical systems theory. Along two curves of Hopf bifurcations an equilibrium loses stability ($U_0 \geq 12.5$ m/s) and gives birth to two distinct families of periodic orbits. These periodic orbits bifurcate into strange attractors along three routes to chaos: period doubling cascades, breakdown of 2-tori by homo- and heteroclinic bifurcations, or intermittency ($U_0 \geq 14.5$ m/s and $h_0 \geq 800$ m).

The observed attractors exhibit spatial and temporal low-frequency patterns comparing well with those observed in the atmosphere. For $h_0 \leq 800$ m the periodic orbits have a period of about 10 days and patterns in the vorticity field propagate eastward. For $h_0 \geq 800$ m, the period is longer (30-60 days) and patterns in the vorticity field are non-propagating. The dynamics on the strange attractors are associated with low-frequency variability: the vorticity fields show weakening and amplification of non-propagating planetary waves on time scales of 10-200 days. The spatio-temporal characteristics are "inherited" (by intermittency) from the two families of periodic orbits and are detected in a relatively large region of the parameter plane. This scenario differs fundamentally from those proposed in the literature so far, which mainly rely on theories involving multiple equilibria.

Key words: atmospheric dynamics, low-frequency variability, low-order models, bifurcations, intermittency, routes to chaos
2010 MSC: 37N10, 37G35, 37D45, 76B60

---

1. Introduction

Weather and climate are complex natural systems since they involve many temporal and spatial scales and a large number of physical processes. In this paper we restrict our attention to large-scale atmospheric flows on time scales of several days to weeks.

1.1. Statement of the problem

A classical problem in the theory of General Atmospheric Circulation is the characterisation of the recurrent flow patterns observed at midlatitudes in the northern hemisphere winters [25]. This issue has been subject of much scientific attention at least since Baur's definition of *Grosswetterlagen* [2], or Rex's description of Atlantic blocking [56]. One of the motivations for the interest is the potential importance of this problem to understand persistence and predictability of atmospheric motion beyond the timescales of baroclinic

synoptic disturbances (2 to 5 days). Indeed, it is expected that insight in the nature of *low-frequency regime dynamics* will lead to significant progress in the so-called extended range weather forecasting [55]. At the same time, the problem is of great relevance in climate science, since it has been proposed that climate change predominantly manifests itself through changes in the atmospheric circulation regimes, that is "changes in the PDF (probability distribution function) of the climate attractor" [19]. As a matter of fact, severe misrepresentation of blocking statistics is widespread in current climate models [50]: this may have a profound impact on the ability of such models to reproduce both current climate and climate change.

A very old idea is to associate recurrent flow patterns with stationary states of the large-scale atmospheric circulation. Such stationary states would correspond to equilibria in the dynamical equations of atmospheric motion. Small-scale weather would then act as a sort of random perturbation inducing fluctuations around equilibria and transitions between states. However, the scientific debate is still very much open on whether a single equilibrium [48, 60] or multiple equilibria [6, 18, 34, 47, 58] actually occur. Hansen and Sutera [33] find bimodality in the statistical distribution of planetary wave activity in observed data. Orographic resonance theories lend support to the hypothesis that activity of planetary waves possesses a multimodal distribution.

A seminal paper in this direction was that by Charney and DeVore in 1979 [18]: they proposed that the interaction between zonal flow and wave field via form-drag explains the occurrence of multiple (two, to be precise) equilibria for the amplitude of planetary waves. This idea has been further elaborated by Legras and Ghil [40] who found intermittent transitions between multiple equilibria respresenting blocked and zonal flows. Crommelin and coworkers [20, 21, 22] explain this behaviour in terms of homo- and heteroclinic dynamics. A limitation of the theories based on barotropic models is that the transitions between the quasi-stable equilibria either involve variations of the zonal wind which of the order of 40 m/s (much larger than in reality [5, 44]), or require unrealistically low orography (200m). It has been known since Charney and Eliassen's work [17] that the interaction between eddy field and orography on planetary scales is characterised by a non-propagating amplification of the eddy field: this is one of the common features observed in many studies of transitions between regimes (see e.g. [46] and references therein). More recent efforts [45] aimed to develop a theory allowing for multiple stable equilibria at the same zonal wind speed, in such

a way that the amplitudes of the corresponding ultralong (planetary scale) waves differ by values of the order of 100 m of geopotential height.

In this paper we adopt a different strategy, involving a shallow water model instead of the more traditional quasi-geostrophic models. The advantage is that physically relevant values can be examined for the parameter representing orography: this parameter, indeed, is bound to be small in quasi-geostrophic models, due to the perturbative nature of orography in quasi-geostrophic theory (see e.g. [1]). Here, a low-order model is derived from the two-layer shallow water equations, where each layer has a constant density and a variable thickness. This reduced model provides a highly simplified model for the atmospheric circulation. The dynamical equations of the 2-layer shallow water model are given by a system of 6 partial differential equations for the fields u_ℓ, v_ℓ, and h_ℓ for $\ell = 1, 2$, where the thickness in layer ℓ is denoted by h_ℓ and the horizontal velocity field is denoted by (u_ℓ, v_ℓ). The model is forced by relaxation to an apparent westerly wind and includes orography in the bottom layer. The low-order model is obtained by expanding the fields u_ℓ, v_ℓ, and h_ℓ in Fourier modes satisfying the boundary conditions. Only Fourier modes with lowest wave numbers are retained in this Fourier expansion. By an orthogonal projection we obtain ordinary differential equations for the time-dependent Fourier coefficients. The orography height and the forcing wind strength are controlled by parameters h_0 and U_0 respectively, which are used for bifurcation analysis in the numerical investigation of the low-order model.

1.2. Summary of the results

The dynamics of the model is stationary for $U_0 \leq 12.2$ m/s and every value of h_0, due to the presence of a stable equilibrium. This equilibrium corresponds to a steady westerly wind with meanders due to interaction with the orography. This steady flow becomes unstable through mixed baroclinic/barotropic instabilities (represented by Hopf bifurcations) as the forcing U_0 increases. This gives rise to two distinct types of stable waves: for lower orography (about 800 m), the period is about 10 days and there is eastward propagation in the bottom layer; for more pronounced orography, the period is longer (30-60 days) and the waves are non-propagating. These waves remain stable in relatively large parameter domains and bifurcate into strange attractors through a number of scenarios (see below) roughly for $U_0 \geq 14.5$ m/s and $h_0 \geq 850$ m. The dynamics on these strange attractors is associated with irregularly recurring flow patterns. Characteristic time

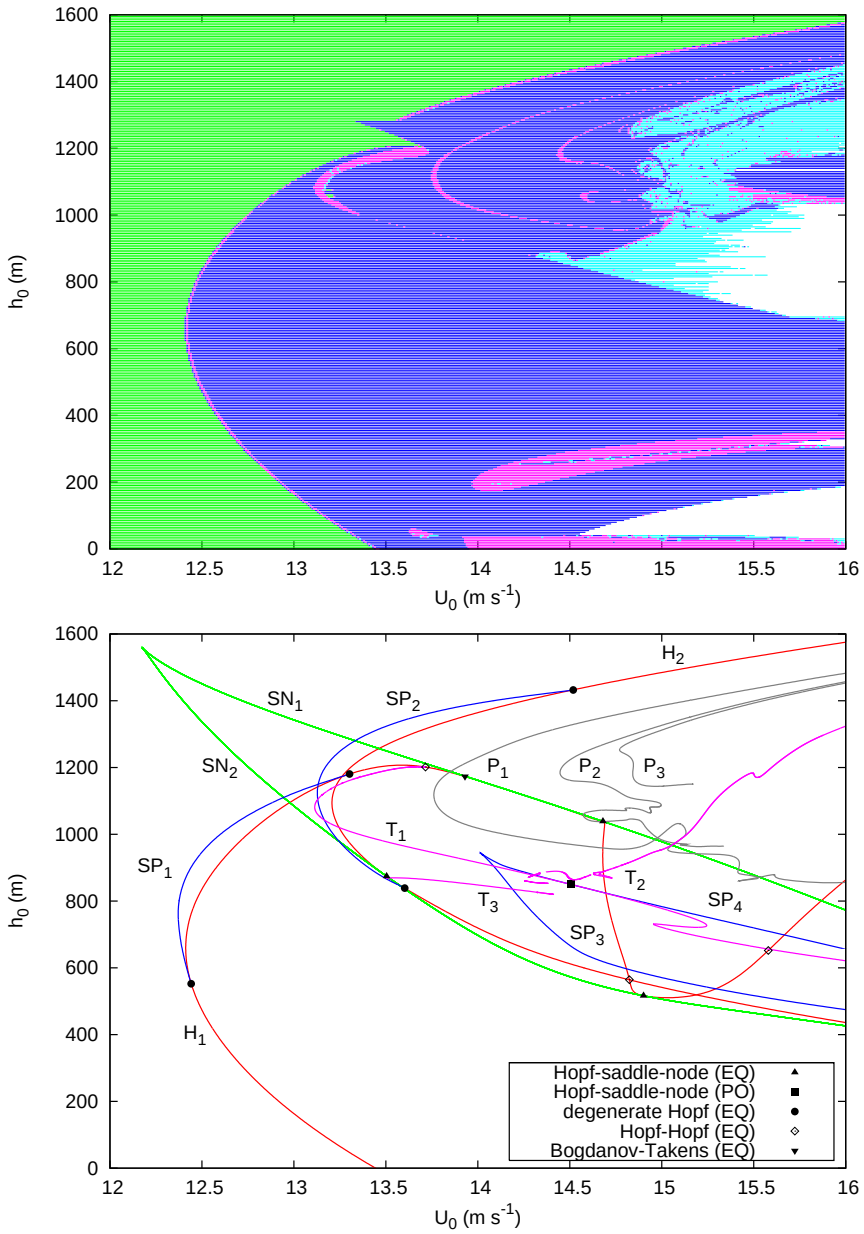

Figure 1: Top: Lyapunov diagram for the attractors of the system. Bottom: bifurcation diagram of attractors of the low-order model in the (U_0, h_0) parameter plane (same parameter window as above). The marked locations are codimension-2 bifurcations. See Table 1 for the colour coding.

Colour	Lyapunov exponents	Attractor type
green	$0 > \lambda_1 \geq \lambda_2 \geq \lambda_3$	equilibrium
blue	$\lambda_1 = 0 > \lambda_2 \geq \lambda_3$	periodic orbit
magenta	$\lambda_1 = \lambda_2 = 0 > \lambda_3$	2-torus
cyan	$\lambda_1 > 0 \geq \lambda_2 \geq \lambda_3$	strange attractor
white		escaping orbit
Colour	Bifurcation type	Bifurcating attractor
green	saddle-node bifurcation	equilibrium
red	Hopf bifurcation	equilibrium
magenta	Hopf-Neĭmark-Sacker bifurcation	periodic orbit
grey	period doubling bifurcation	periodic orbit
blue	saddle-node bifurcation	periodic orbit

Table 1: Colour coding for the Lyapunov diagram and bifurcation diagram in Figure 1.

scales are in the range of 10-200 days, where the lower frequency components (60-200 days) can be interpreted as harmonics of the higher frequency components (10-60 days). In addition, patterns in the vorticity field are inherited from the periodic orbit that gives birth to the strange attractor.

The Lyapunov diagram (top panel of Figure 1) shows a classification of the dynamical behaviour in the different regions of the (U_0, h_0)-plane. Bifurcations of equilibria and periodic orbits (bottom panel) explain the main features of the Lyapunov diagram. The two Hopf curves $H_{1,2}$ give birth to stable periodic orbits. In turn, these periodic orbits bifurcate into strange attractors through three main routes to chaos:

- Period doubling cascade of periodic orbits (the curves $P_{1,2,3}$);
- Hopf-Neĭmark-Sacker bifurcation of periodic orbits (the curve T_2), followed by the breakdown of a 2-torus;
- Saddle-node bifurcation of periodic orbits taking place on a strange attractor (the curve SP_4), the so-called intermittency route [51].

These routes have been detected in many studies of low-order atmospheric models [11, 40, 43, 61, 63].

An outline of the rest of the paper is now given. The derivation of the low-order model from the 2-layer shallow water equations is presented in Section 2. The bifurcation diagram of the low-order model is discussed in

Section 3.1, followed by analysis of the routes to chaos in Section 3.2. Some remarks on the involved mathematics are made in Section 3.3. Finally, the interpretation of our results in terms of atmospheric low-frequency variability is given in Section 3.4.

2. Model

We consider atmospheric flow in two layers. In each layer the velocity field (u, v) is 2-dimensional. The thickness h of each layer is variable, which is the only 3-dimensional aspect of this model. The governing equations are given by a system of six partial differential equations. By means of truncated Fourier expansions and a Galerkin projection we obtain a low-order model which consists of a 46-dimensional system of ordinary differential equations.

2.1. The 2-layer shallow water equations

The constants H_1 and H_2 denote the mean thickness of each layer, and the fields η_1' and η_2' denote deviations from the mean thickness, where primes indicate that the variable is dimensional. The thickness fields of the two layers are given by

$$h_1' = H_1 + \eta_1' - \eta_2', \tag{1}$$
$$h_2' = H_2 + \eta_2' - h_b', \tag{2}$$

where h_b denotes the bottom topography profile; see Figure 2. The pressure fields are related to the thickness fields by means of the hydrostatic relation

$$p_1' = \rho_1 g(h_1' + h_2' + h_b'), \tag{3}$$
$$p_2' = \rho_1 g h_1' + \rho_2 g(h_2' + h_b'), \tag{4}$$

where the constants ρ_1 and ρ_2 denote the density of each layer.

The governing equations are nondimensionalised using scales L, U, L/U, D, and $\rho_0 U^2$ for length, velocity, time, depth, and pressure, respectively, and

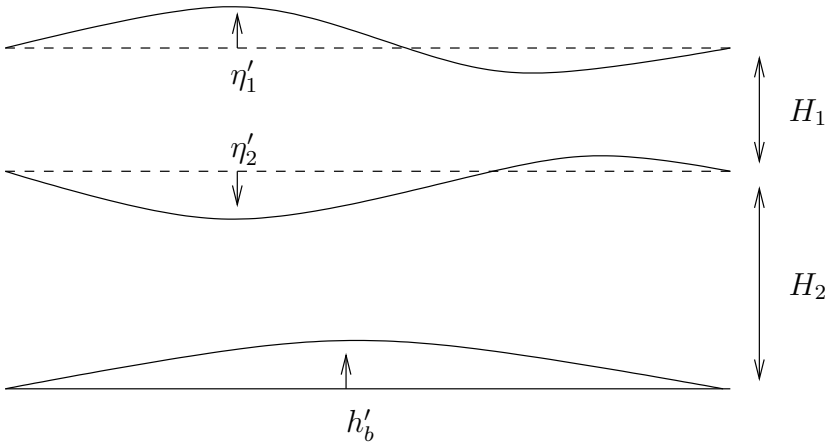

Figure 2: Layers in the shallow water model.

are given by

$$\begin{aligned}
\frac{\partial u_\ell}{\partial t} + u_\ell \frac{\partial u_\ell}{\partial x} + v_\ell \frac{\partial u_\ell}{\partial y} &= -\frac{\partial p_\ell}{\partial x} + (Ro^{-1} + \beta y) v_\ell \\
&\quad - \sigma\mu(u_\ell - u_\ell^*) + Ro^{-1} E_H \Delta u_\ell - \sigma r \delta_{\ell,2} u_\ell \\
\frac{\partial v_\ell}{\partial t} + u_\ell \frac{\partial v_\ell}{\partial x} + v_\ell \frac{\partial v_\ell}{\partial y} &= -\frac{\partial p_\ell}{\partial y} - (Ro^{-1} + \beta y) u_\ell \\
&\quad - \sigma\mu(v_\ell - v_\ell^*) + Ro^{-1} E_H \Delta v_\ell - \sigma r \delta_{\ell,2} v_\ell \\
\frac{\partial h_\ell}{\partial t} + u_\ell \frac{\partial h_\ell}{\partial x} + v_\ell \frac{\partial h_\ell}{\partial y} &= -h_\ell \left(\frac{\partial u_\ell}{\partial x} + \frac{\partial v_\ell}{\partial y} \right)
\end{aligned} \tag{5}$$

where u_ℓ and v_ℓ are eastward and northward components of the 2-dimensional velocity field, respectively. In addition, the nondimensional pressure terms are given by

$$\begin{aligned}
p_1 &= \frac{\rho_1}{\rho_0} F(h_1 + h_2 + h_b), \\
p_2 &= \frac{\rho_1}{\rho_0} F h_1 + \frac{\rho_2}{\rho_0} F(h_2 + h_b).
\end{aligned}$$

In the governing equations several nondimensional numbers appear: the advective timescale σ, the nondimensional β-parameter, the Rossby number Ro, the horizontal Ekman number E_H, and the inverse Froude number F. These parameters have the following expressions in terms of the dimensional

parameters:

$$\sigma = \frac{L}{U}, \quad \beta = \frac{\beta_0 L^2}{U}, \quad Ro = \frac{U}{f_0 L}, \quad E_H = \frac{A_H}{f_0 L^2}, \quad F = \frac{gD}{U^2}.$$

Standard values of the dimensional parameters are listed in Table 2.

The dynamical equations will be considered on the zonal β-plane channel

$$0 \le x \le L_x/L, \quad 0 \le y \le L_y/L.$$

Suitable boundary conditions have to be imposed: we require all fields to be periodic in the x-direction. At $y = 0, L_y/L$ we impose the conditions

$$\frac{\partial u_\ell}{\partial y} = \frac{\partial h_\ell}{\partial y} = v_\ell = 0.$$

The model is forced by relaxation to an apparent westerly wind given by the profile

$$\begin{aligned} u_1^*(x,y) &= \alpha_1 U_0 U^{-1}(1 - \cos(2\pi y L/L_y)), \quad v_1^*(x,y) = 0, \\ u_2^*(x,y) &= \alpha_2 U_0 U^{-1}(1 - \cos(2\pi y L/L_y)), \quad v_2^*(x,y) = 0, \end{aligned}$$

where the dimensional parameter U_0 controls the strength of the forcing and the nondimensional parameters α_1 and α_2 control the vertical shear of the forcing. For the bottom topography we choose a profile with zonal wave number 3:

$$h_b(x,y) = h_0 D^{-1}(1 + \cos(6\pi x L/L_x)),$$

where the dimensional parameter h_0 controls the amplitude of the topography. We require that the bottom topography is contained entirely in the bottom layer which implies the restriction $h_0 \le H_2/2$.

2.2. The low-order model

The governing equations in (5) form a dynamical system with an infinite-dimensional state space. We reduce the infinite-dimensional system to a system of finitely many ordinary differential equations by means of a Galerkin projection. This amounts to an expansion of the unknown fields u_ℓ, v_ℓ, h_ℓ in terms of known basis functions, depending only on spatial variables, with unknown coefficients, depending only on time. An orthogonal projection onto the space spanned by the basis functions gives a set of finitely many ordinary differential equations for the expansion coefficients.

Parameter	Meaning	Value	Unit
A_H	momentum diffusion coefficient	1.0×10^2	$\mathrm{m^2\,s^{-1}}$
μ	relaxation coefficient	1.0×10^{-6}	$\mathrm{s^{-1}}$
r	linear friction coefficient	1.0×10^{-6}	$\mathrm{s^{-1}}$
f_0	Coriolis parameter	1.0×10^{-4}	$\mathrm{s^{-1}}$
β_0	planetary vorticity gradient	1.6×10^{-11}	$\mathrm{m^{-1}\,s^{-1}}$
ρ_0	reference density	1.0	$\mathrm{kg\,m^{-3}}$
ρ_1	density (top layer)	1.01	$\mathrm{kg\,m^{-3}}$
ρ_2	density (bottom layer)	1.05	$\mathrm{kg\,m^{-3}}$
g	gravitational acceleration	9.8	$\mathrm{m\,s^{-2}}$
α_1	zonal velocity forcing strength (top layer)	1.0	
α_2	zonal velocity forcing strength (bottom layer)	0.5	
L_x	channel length	2.9×10^7	m
L_y	channel width	2.5×10^6	m
H_1	mean thickness (top layer)	5.0×10^3	m
H_2	mean thickness (bottom layer)	5.0×10^3	m
L	characteristic length scale	1.0×10^6	m
U	characteristic velocity scale	1.0×10^1	$\mathrm{m\,s^{-1}}$
D	characteristic depth scale	1.0×10^3	m

Table 2: Standard values of the fixed parameters.

As basis functions we will use the Fourier modes with half wave numbers. For an integer $k \geq 0$ and a real number $\alpha > 0$ these functions are given by

$$c_k(\xi;\alpha) := \begin{cases} \dfrac{1}{\sqrt{\alpha}} & k = 0 \\ \sqrt{\dfrac{2}{\alpha}} \cos\left(\dfrac{k\pi\xi}{\alpha}\right) & k > 0, \end{cases} \qquad (6)$$

$$s_k(\xi;\alpha) := \sqrt{\frac{2}{\alpha}} \sin\left(\frac{k\pi\xi}{\alpha}\right),$$

where $\xi \in [0, \alpha]$, and the numerical factors serve as normalisation constants.

Deciding which Fourier modes to retain in the Galerkin projection is a non-trivial problem. A priori it is not known which choice captures the dynamics of the infinite-dimensional system in the best possible way. In [52, 53, 54] this problem has been addressed in the setting of a Rayleigh-Bénard convection problem by checking qualitative changes in dynamical behaviour and quantitative information on the location of branches of equilibria and their bifurcations, while increasing the number of retained modes. Such an approach is beyond the scope of the present paper, and here we choose an ad hoc approach. In [6] it was shown that atmospheric low-frequency behaviour manifests itself at zonal wavenumbers less than 5. To keep the dimension of the low-order model as low as possible we only retain the wave numbers $m = 0, 3$ in the zonal direction, and the wave numbers $n = 0, 1, 2$ in the meridional direction. Let

$$R = \{(0,0), (0,1), (0,2), (3,0), (3,1), (3,2)\}$$

denote the set of retained wave number pairs. Moreover, set $a = L_x/L$ and $b = L_y/L$. Then all nondimensional fields are expanded as

$$u_\ell(x,y,t) = \sum_{(m,n)\in R} \left[\widehat{u}^c_{\ell,m,n}(t) c_{2m}(x;a) + \widehat{u}^s_{\ell,m,n}(t) s_{2m}(x;a)\right] c_n(y;b),$$

$$v_\ell(x,y,t) = \sum_{(m,n)\in R} \left[\widehat{v}^c_{\ell,m,n}(t) c_{2m}(x;a) + \widehat{v}^s_{\ell,m,n}(t) s_{2m}(x;a)\right] s_n(y;b),$$

$$h_\ell(x,y,t) = \sum_{(m,n)\in R} \left[\widehat{h}^c_{\ell,m,n}(t) c_{2m}(x;a) + \widehat{h}^s_{\ell,m,n}(t) s_{2m}(x;a)\right] c_n(y;b).$$

In this way the truncated expansions satisfy the boundary conditions.

By substituting the truncated expansions in (5) and projecting (with respect to the standard inner product) the governing equations on the Fourier modes, we obtain a system of ordinary differential equations for the time-dependent Fourier coefficients. With the above choice of the retained wavenumbers, we need 9, 6, and 9 coefficients for the fields u_ℓ, v_ℓ, and h_ℓ, respectively. However, due to conservation of mass, it turns out that the coefficients $\widehat{h}_{\ell,0,0}$ are constant in time and therefore they can be treated as a constant. Hence, the low-order model is 46-dimensional. Formulas to compute the coefficients of the low-order model are presented in Appendix B.

3. Results

We here investigate the dynamics of the low-order model, starting from a description of the bifurcations in Figure 1 (Section 3.1). It is shown how low-frequency dynamical behaviour is linked to strange attractors, which occur in a relatively large parameter domain. The onset of chaotic dynamics is explained in terms of bifurcation scenarios ("routes to chaos", Section 3.2). Lastly, physical interpretation of the dynamics is given in terms of atmospheric low-frequency variability (Section 3.4).

3.1. Organisation of the parameter plane

In this section we give a detailed description of the bifurcation diagram and we explain how this clarifies various parts of the Lyapunov diagram. The bifurcations detected in our model are standard, and they are discussed in detail in, e.g., [39].

Lyapunov diagram. The top panel of Figure 1 contains the Lyapunov diagram of the attractors of the low-order model. This is produced by scanning the (U_0, h_0)-parameter plane from left to right and classifying the detected attractor by means of Lyapunov exponents, see [12, 13] for details. Along each line of constant h_0 we start with a fixed initial condition when $U_0 = 12$ m/s. For the next parameter values on this line we take the last point of the previous attractor as an initial condition for the next one.

We do not exclude the possibility of coexisting attractors, but this can not be detected by our procedure. By means of more refined procedures, with varying initial conditions, coexistence of attractors can be detected as well. For large values of the parameter U_0 orbits can escape to infinity (see the white parts in Figure 1), but this also depends on the chosen initial condition. These unbounded orbits have also been detected in [42].

Bifurcations of equilibria. The transition from stationary to periodic behaviour in the Lyapunov diagram (Figure 1) is explained by Hopf bifurcations where an equilibrium loses stability. A stable equilibrium is found for $U_0 = 0$ m/s and remains stable up to $U_0 = 12.2$ m/s. The equilibrium undergoes one or more Hopf bifurcations for $U_0 > 12.2$ m/s approximately: loss of stability occurs at curves H_1 and H_2 in Figure 1 (we only focus on bifurcations leading to loss of stability here). Periodic orbits born at the H_1 curve have periods of about 10 days, whereas periodic orbits born at the H_2 curve have periods in the range of 30 – 60 days; see Figure 3 and Figure 4, respectively[1].

A pair of degenerate Hopf points occur at the tangencies between the Hopf curves $H_{1,2}$ and the curves SP_1 and SP_2 of saddle-node bifurcations of periodic orbits. The bifurcation type on $H_{1,2}$ changes from supercritical to subcritical at the degenerate Hopf points. Two branches of stable periodic orbits are thus formed on either of $SP_{1,2}$ or $H_{1,2}$.

Two curves SN_1 and SN_2 of saddle-node bifurcations of equilibria meet in a cusp. This leads to a domain in the parameter plane for which three equilibria coexist. The boundaries of this domain are tangent to the Hopf curves H_1 and H_2 at three different Hopf-saddle-node bifurcation points. Moreover, a Bogdanov-Takens point occurs along one of the saddle-node curves, where one additional real eigenvalue crosses the imaginary axis.

Bifurcations of periodic orbits born at H_1 or SP_1. The periodic orbits born at the curves H_1 or SP_1 lose stability through either Hopf-Neĭmark-Sacker or saddle-node bifurcations. The Hopf-Neĭmark-Sacker curve T_1 originates from a Hopf-Hopf point at the curve H_1, where two pairs of complex eigenvalues cross the imaginary axis. The saddle-node curves $SP_{3,4}$ are joined in a cusp, and the curve SP_4 forms part of a boundary between periodic and chaotic behaviour in the Lyapunov diagram. Moreover, the curve SP_4 becomes tangent to the Hopf-Neĭmark-Sacker curve T_1 at a Hopf-saddle-node bifurcation point of periodic orbits.

Bifurcations of periodic orbits born at H_2 or SP_2. The periodic orbits born at the curves H_2 or SP_2 may lose stability through either a period doubling bifurcation or Hopf-Neĭmark-Sacker bifurcations. The former occurs on curve

[1]Unless specified otherwise, attractors are plotted on directions of maximal amplitude. See Section A.3 for details. Since the projection is computed numerically, labels for the axes are omitted.

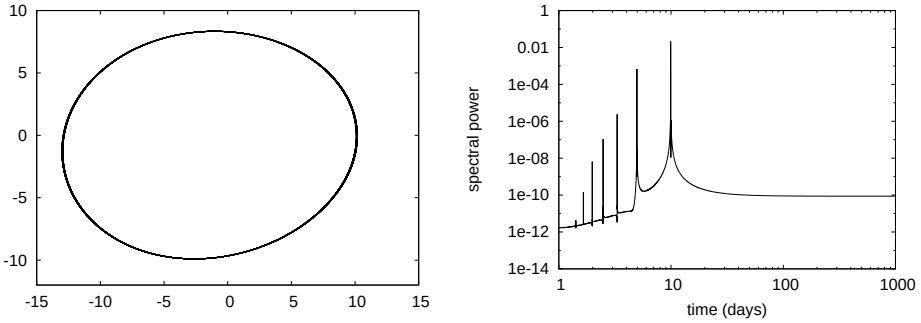

Figure 3: Periodic orbit born at Hopf bifurcation H_1 ($U_0 = 13.32$ m/s, $h_0 = 800$ m) and its power spectrum. The period is approximately 10 days.

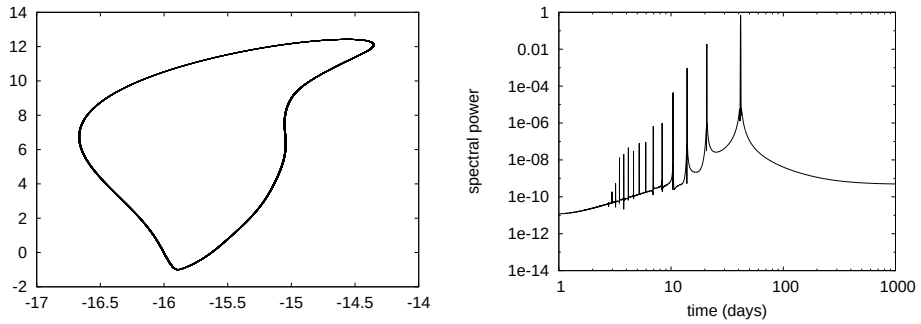

Figure 4: Periodic orbit born at Hopf bifurcation H_2 ($U_0 = 14.64$ m/s, $h_0 = 1400$ m) and its power spectrum. The period is approximately 60 days.

P_1, which is the first of a cascade leading to a chaotic attractor, see the next section. Hopf-Neĭmark-Sacker bifurcations occur on curves T_2 and T_3 in Figure 1: T_2 originates from a Hopf-saddle-node bifurcation point of periodic orbits, and T_3 is tangent to the period doubling curve P_1 at a 1:2-resonance point.

3.2. Routes to chaos

We have identified three different routes from orderly to chaotic behaviour. All of them involve one or more bifurcations of the stable periodic orbits described in the previous section.

Period doublings. The periodic orbits born at the Hopf bifurcation H_2 lose stability through a period doubling bifurcation (see previous section). Three period doubling curves $P_{1,2,3}$ are shown in Figure 1, and we expect that they

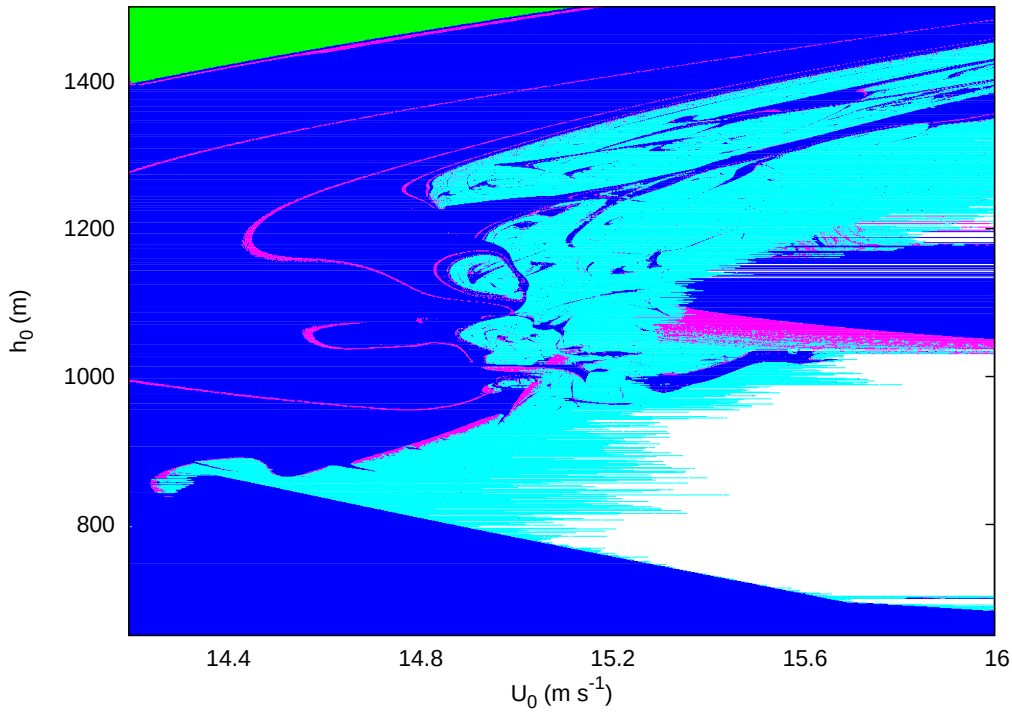

Figure 5: Magnification of the Lyapunov diagram in Figure 1; see Table 1 for the colour coding.

are the first of an infinite cascade. Indeed, a magnification of the Lyapunov diagram (Figure 5) reveals a large chaotic region at the right of P_3, interrupted by narrow domains of periodic behaviour. Occurrence of these windows of periodicity is confirmed in the diagrams in Figure 6. However, these gaps disappear for lower values of the parameter h_0, and chaotic behaviour seems to be persistent on a continuum.

Figure 7 shows a twice-doubled stable periodic orbit along the cascade and a strange attractor after the end of the cascade. The dynamics on the strange attractor exhibits low-frequency behaviour in the range 20-200 days (see the power spectrum in Figure 7). The peaks around 100 and 200 days are 'inherited' from the twice-doubled periodic orbit. In turn, these originate from the same branch of periodic orbits as in Figure 4: just before the first period doubling bifurcation P_1 ($U_0 = 13.9$ m/s, $h_0 = 1200$ m) this stable periodic orbit has a period of approximately 50 days (not shown).

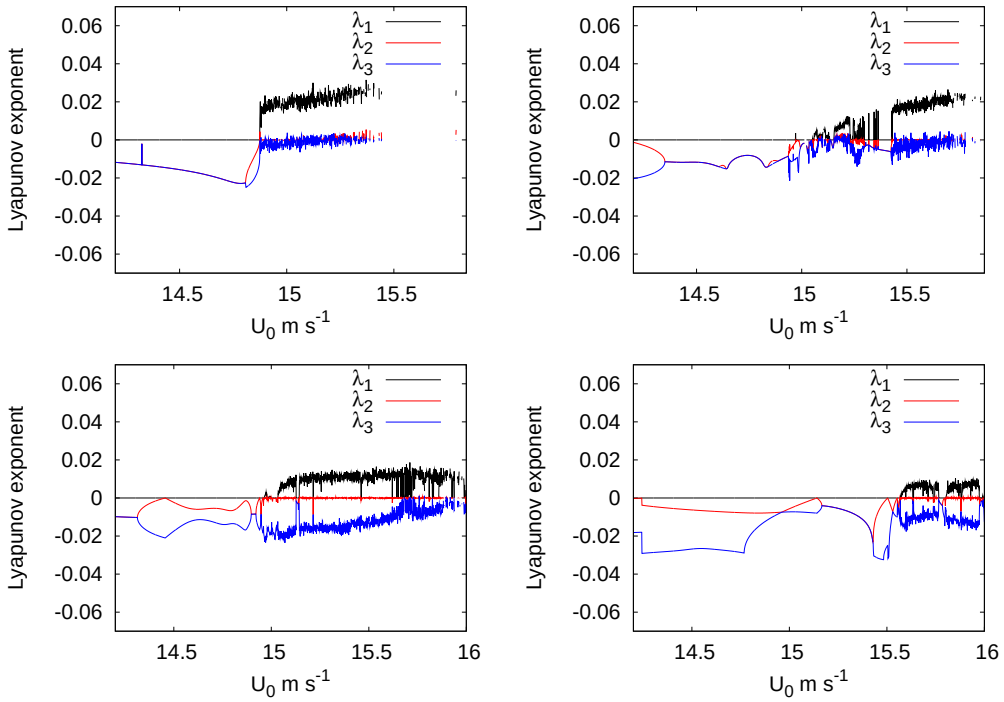

Figure 6: The three largest Lyapunov exponents $\lambda_1 \geq \lambda_2 \geq \lambda_3$ (non-dimensional) as a function of U_0. The value of the parameter h_0 is fixed at $h_0 = 800$ m (top left), $h_0 = 1000$ m (top right), $h_0 = 1200$ m (bottom left), and $h_0 = 1400$ m (bottom right).

Broken torus. Two-torus attractors occur in a narrow region separating periodic from chaotic behaviour in the Lyapunov diagram (Figure 5). The 2-torus attractors branch off from periodic orbits at the Hopf-Neĭmark-Sacker bifurcations on curve T_2. The periodic orbits losing stability here belong to the branch created at the Hopf curve H_2 (see previous section). The 2-torus attractors quickly break down giving rise to a strange attractor (Figure 8). This strange attractor exhibits low-frequency behaviour in the range 10-100 days. The main spectral peaks at 56 and 11 days are inherited from the 2-torus, which has two frequencies $\omega_1 = 0.0178$ days^{-1} and $\omega_2 = 0.0888$ days^{-1} for parameters right after the Hopf-Neĭmark-Sacker bifurcation. In turn the torus inherits one of the frequencies from the periodic orbit, which has a period of approximately 56 days just before the Hopf-Neĭmark-Sacker bifurcation ($U_0 = 14.74$ m/s, $h_0 = 900$ m, not shown).

The process leading to the creation of the above strange attractor involves

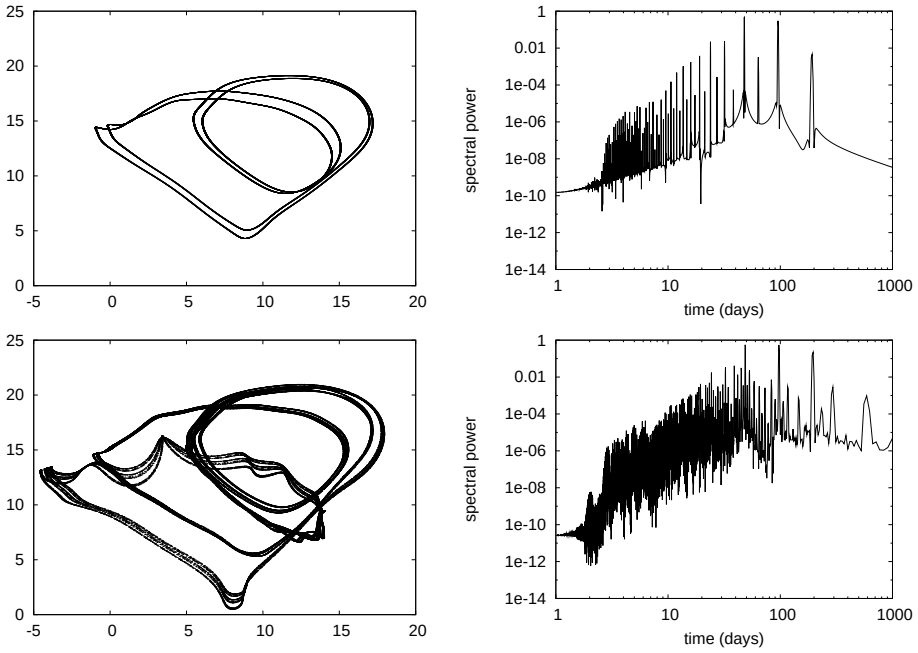

Figure 7: Attractors (left panels, same projection) and their power spectra (right) for $h_0 = 1200$ m. Top: periodic orbit after two period doublings ($U_0 = 14.48$ m/s). Bottom: strange attractor after a period doubling cascade ($U_0 = 15$ m/s).

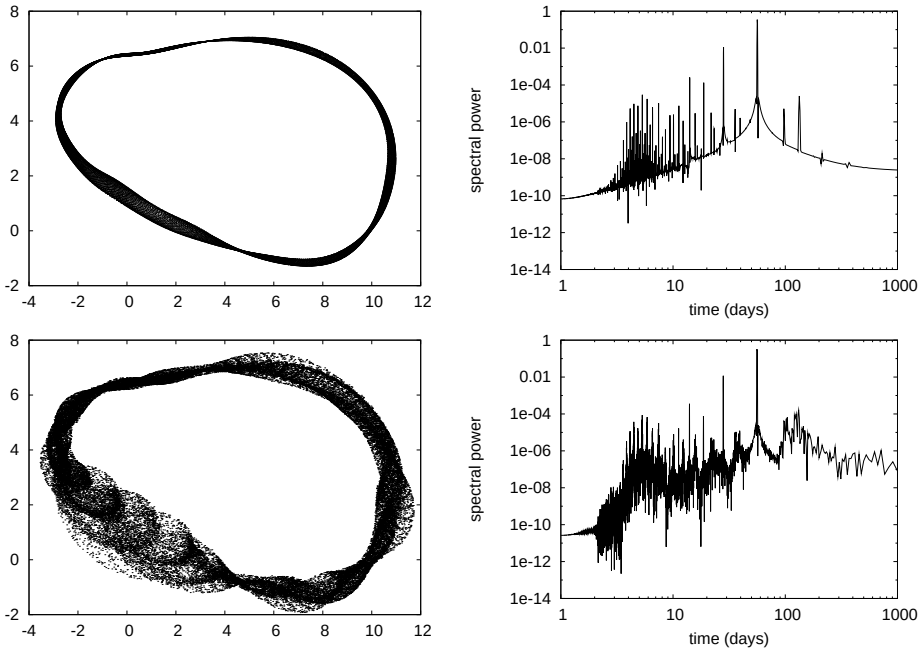

Figure 8: Same as Figure 7 for $h_0 = 900$ m: a 2-torus attractor (top, $U_0 = 14.75$ m/s) and a strange attractor after the 2-torus breakdown (bottom, $U_0 = 14.78$ m/s).

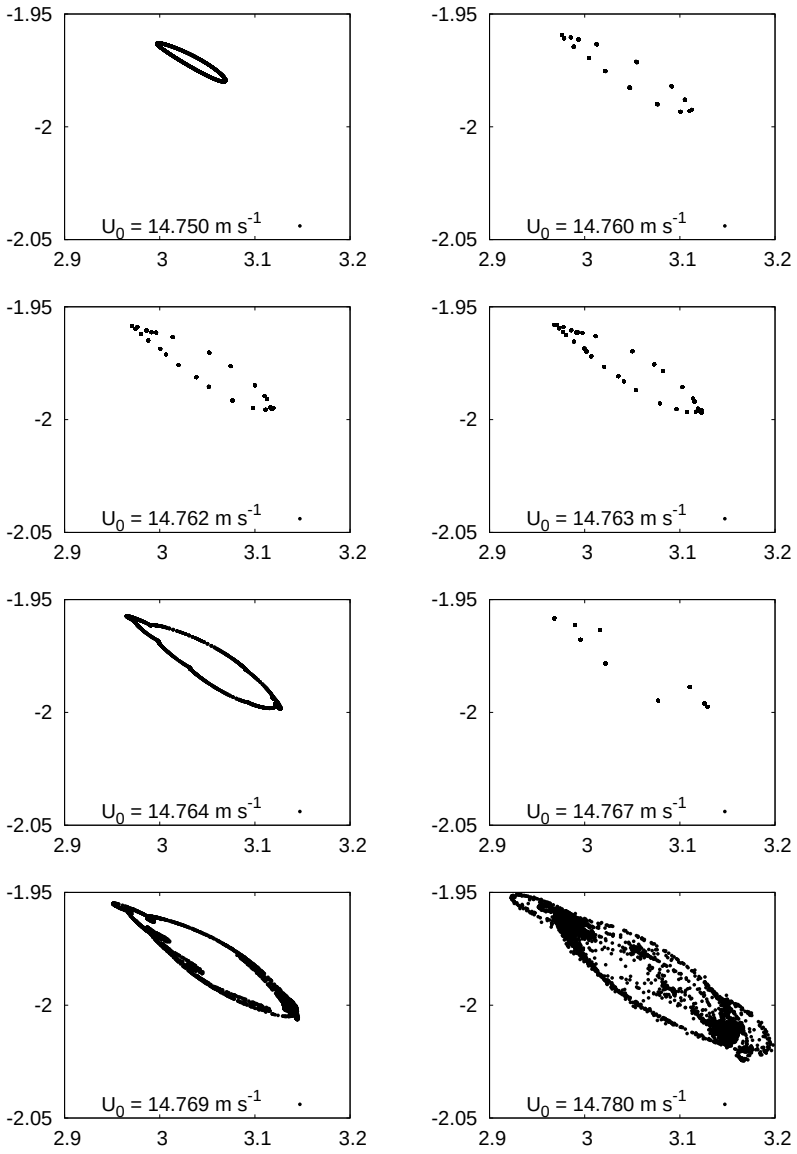

Figure 9: Breakdown of the 2-torus attractor, visualised in the Poincaré section $\widehat{u}_{2,0,0} = 1.8$, projection on $(\widehat{u}_{2,0,1}, \widehat{u}_{2,0,2})$: alternation of periodic, quasi-periodic, and chaotic dynamics as the parameter U_0 is varied with constant $h_0 = 900$ m.

transition through a number of phase-locking windows as U_0 is increased. Figure 9 shows Poincaré sections for $U_0 = 14.750$ m/s up to $U_0 = 14.780$ m/s with step 0.001 m/s with $h_0 = 900$ m fixed. Densely filled invariant circles and periodic points in the Poincaré section correspond to quasi-periodic 2-tori and periodic orbits of the flow, respectively. Periodicity windows with with periods 16, 25, 34, 9, and 11 are crossed as U_0 is increased, until the invariant circle breaks up and the quasi-periodic dynamics is replaced by chaotic dynamics. The size of the attractor is growing rapidly in phase space as U_0 is changed. The breakdown of a 2-torus often involves homo- and heteroclinic bifurcations; see Section 3.3 for details.

Intermittency. The saddle-node curve SP_4 in Figure 1 forms one of the boundaries between the regions of periodic and chaotic behaviour in the Lyapunov diagram. Figure 10 (top left panel) shows a stable periodic orbit born at the curve SP_1; the period is 10 days. When the parameters cross the saddle-node curve SP_4, the stable periodic disappears and a strange attractor is found; see Figure 10 (bottom left panel).

The dynamics on the attractor seems to consist of a sequence of passages close to heteroclinic orbits between different objects. The attractor coexists with (at least) the following objects.

- An unstable periodic orbit with a 2-dimensional unstable manifold (due to one pair of complex conjugate Floquet multipliers in the right half-plane).
- Three unstable equilibria with unstable manifolds of dimension 4, 3, and 2 (due to two, one, and one pair(s) of complex conjugate eigenvalues in the right half plane, respectively).

Figure 11 shows that the dynamics on the attractor consists of different regimes.

- Regimes of nearly regular periodic behaviour correspond to intermittency near the formerly existing stable periodic orbit, which disappeared through the saddle-node curve SP_4.
- Regimes of nearly stationary behaviour are observed when the orbit approaches one of the three equilibria mentioned above.
- The previous two regimes are alternated with irregular behaviour.

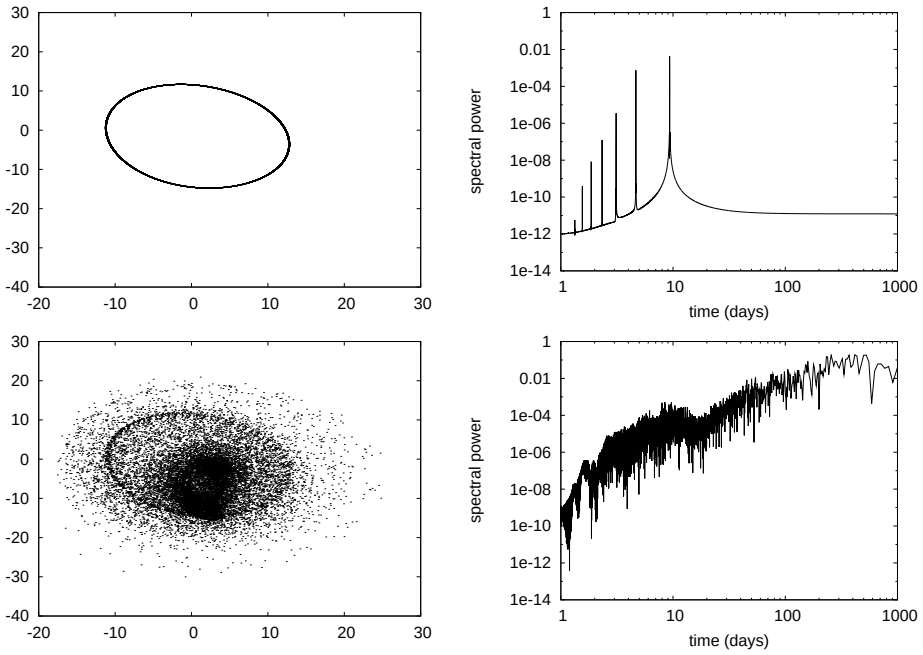

Figure 10: Same as Figure 7 for $h_0 = 800$ m. Top row: stable periodic orbit before the saddle-node bifurcation ($U_0 = 14.87$ m/s). Bottom row: strange attractor after the saddle-node bifurcation ($U_0 = 15$ m/s).

The intermittency regimes often occur directly after the orbit approached one the equilibria, but this is not always the same equilibrium. We have tested this by computing a large number of orbits, for which the initial conditions are random points in the tangent space to the unstable manifold of the equilibrium. The intermittency regime can be reached immediately by starting near the equilibria with the 4-dimensional and 3-dimensional unstable manifolds. When starting near the equilibrium with the 2-dimensional unstable manifold, however, the orbit shows irregular behaviour before reaching the intermittency regime.

Orbits on the attractor never approach the unstable periodic orbit within a small distance. Again we have computed a large number of orbits, for which the initial conditions are random points in the tangent space of the unstable manifold of the periodic orbit. In general, first a long transient of irregular behaviour is observed, and then the orbit reaches the intermittency regime.

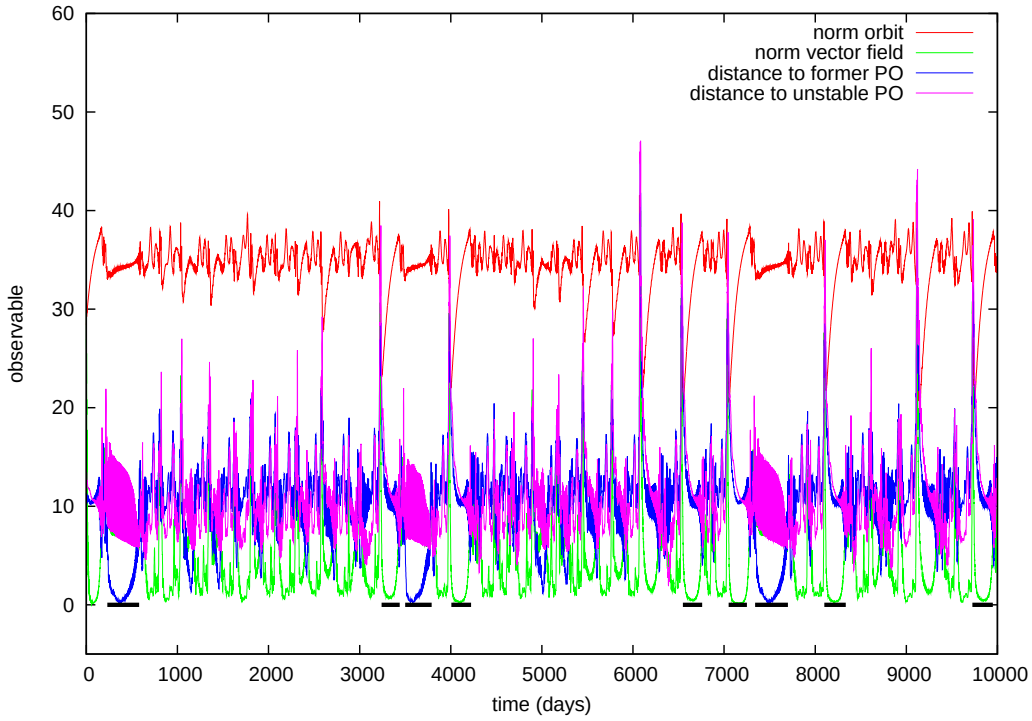

Figure 11: Four time series, derived from one orbit on the attractor in Figure 10 using four different observables: norm of the orbit (red), norm of the vector field along the orbit (green), distance of the orbit to the position of the formerly existing periodic orbit (blue), and distance to the unstable periodic orbit (magenta). Black bars underneath mark time intervals of intermittency near either the periodic orbit or an equilibrium.

3.3. Theoretical remarks

The results of the previous subsections are now interpreted in terms of known theory.

Bifurcations of equilibria and periodic orbits. The codimension-1 bifurcations of equilibria and periodic orbits we have found are standard and have been described extensively in the literature; see, for instance, [7, 16, 32, 39] and the references therein. For each bifurcation a (truncated) normal form can be derived by restricting the vector field to an approximation of a centre manifold. This normal form can be used to check the appropriate genericity and transversality conditions and to study different unfolding scenarios. This methodology is described in detail in [39], see [59] for other methods of computing normal forms.

The codimension-2 bifurcations of equilibria (Bogdanov-Takens, Hopf-Hopf, and Hopf-saddle-node) have been described in detail in [39]. In this case, however, the truncated normal forms only provide partial information on the dynamics near the bifurcation. The Hopf-saddle-node bifurcation for diffeomorphisms has been studied extensively in [12, 13].

Period doubling route. This scenario for the birth of strange attractors is theoretically well-understood, see for example [10, 23] and references therein. Strange attractors obtained from infinite period doublings in one direction may be reached at once by homo- and heteroclinic tangencies from another direction [49]. When curves of period doubling bifurcations form unnested islands, the chaotic region can be reached by a variety of routes, including the breakdown of a 2-torus or the sudden appearance of a chaotic attractor [64].

2-tori and their breakdown. It is well known that 2-torus attractors of dissipative systems generically occur as families of quasi-periodic attractors parameterised over a Cantor set (of positive 1-dimensional Hausdorff measure) in a Whitney-smooth way, see [7, 8, 16]. These attractors are often a transient stage between periodic and chaotic dynamics.

The birth and death of periodic orbits on an invariant torus occur when the parameters move across Arnol′d resonance tongues. These are regions in the parameter plane bounded by pairs of curves of saddle-node bifurcations originating from a common resonant Hopf-Neĭmark-Sacker bifurcation. For parameters inside a tongue the dynamics on the torus is phase locked, meaning that the invariant circle of the Poincaré map (defined by a section transversal to the torus) is the union of a stable periodic point and the unstable manifolds of an unstable periodic point (see, for example, the top right panel in Figure 9). The circle can be destroyed by homoclinic tangencies between the stable and unstable manifolds of the unstable periodic point, or the circle can interact with other objects via heteroclinic tangencies. See [9, 10] for an extensive discussion.

Intermittency. The phenomenon of intermittency near a saddle-node bifurcations is well-known, but it only explains a part of the dynamics on the strange attractor in Figure 10. Furthermore, the geometrical structure of the strange attractor remains unclear. In many systems, strange attractors are formed by the closure of the unstable manifold of a saddle-like object. This *Ansatz* is discussed in several works, see e.g. [10, 16] and references therein. However,

the structure of the attractor in Figure 10 seems to be more complicated, involving interaction with several nearby invariant objects (equilibria, periodic orbits) of saddle type.

We consider it as an interesting problem for future research to investigate the structure of the attractor in Figure 10 in more detail. At least the stable and unstable manifolds of the equilibria and the periodic orbit should be computed, in order to gain more insight in the structure of the attractor. Next, the 'genealogy' of the attractor should be determined, e.g., by identifying whether the present shape is created through a sequence of bifurcations. For a more thorough analysis it might be necessary to derive a simpler model for this attractor, having a state space with the lowest possible dimension.

3.4. Physical interpretation

In this section we investigate the physical aspects (mainly instability and wave propagation) associated with the attractors analysed in the previous section. Hopf bifurcations are first interpreted in terms of geophysical fluid dynamical instabilities, giving rise to planetary waves. The structure of these waves is then studied through Hovmöller diagrams of the vorticity field [35]. This allows us to visualise structural differences and changes, such as the onset of large-scale meanders in the westerly wind.

Hopf bifurcations. A fluid is said to be hydrodynamically unstable when small perturbations of the flow can grow spontaneously, drawing energy from the mean flow. At a Hopf bifurcation an equilibrium loses its stability and gives birth to a periodic orbit. In the context of a fluid this can be interpreted as a steady flow becoming unstable to an oscillatory perturbation (such as a travelling wave). Two wave instabilities are well-known in geophysical fluid dynamics: barotropic and baroclinic instabilities. The fundamental difference lies in the source of energy: perturbations derive their energy from the horizontal shear of the mean flow in a barotropically unstable flow. In a baroclinically unstable flow, perturbations derive their kinetic energy from the potential energy of the mean flow associated with the existence of vertical shear in the velocity field. The reader is referred to standard textbooks on geophysical fluid dynamics for a full discussion on this subject [28, 29, 36].

At a Hopf bifurcation the Jacobian matrix of the vector field has two eigenvalues $\pm\omega i$ on the imaginary axis. Let $\Phi_1 \pm i\Phi_2$ denote corresponding eigenvectors, then

$$P(t) = \cos(\omega t)\,\Phi_1 - \sin(\omega t)\,\Phi_2 \tag{7}$$

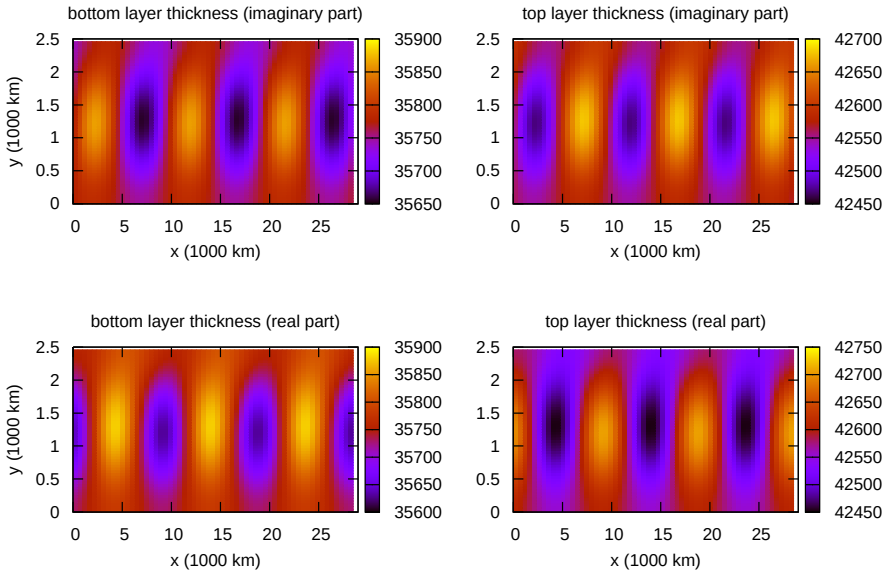

Figure 12: Patterns of layer thickness associated with the eigenvectors at the Hopf bifurcation H_1, for $U_0 = 12.47$ m/s and $h_0 = 800$ m. The scale is arbitrary, since any scalar multiple of (7) is a solution of the linearised vector field.

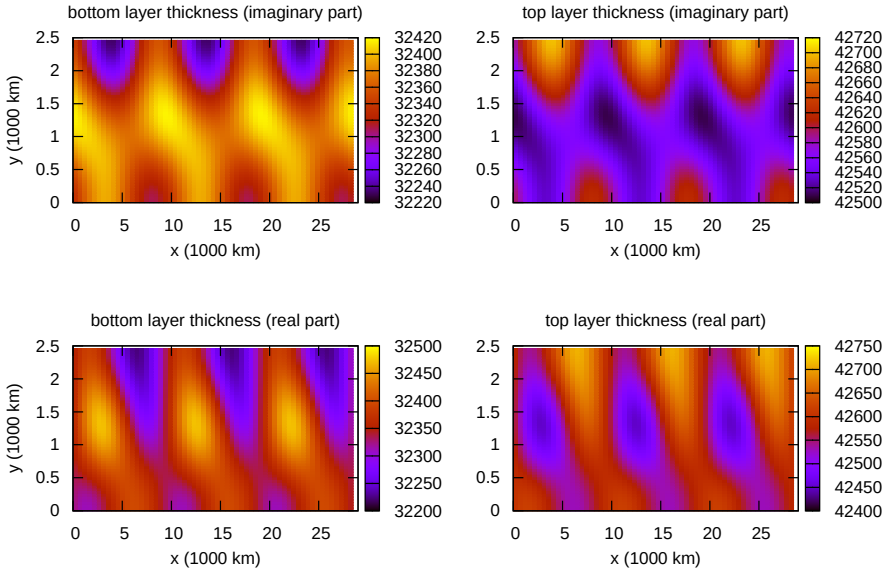

Figure 13: Same as Figure 12 at Hopf curve H_2, for $U_0 = 13.31$ m/s and $h_0 = 1200$ m.

is a periodic orbit of the vector field obtained by linearisation around the equilibrium undergoing the Hopf bifurcation. This can be interpreted as a wave-like response to a perturbation of the equilibrium. The propagation of the physical pattern associated to this wave can be followed by looking at the physical fields at the phases $P(-\pi/2\omega) = \Phi_2$ and $P(0) = \Phi_1$. Figure 12 shows the layer thickness associated with the eigenvectors at the Hopf bifurcation H_1. Clearly, positive and negative anomalies are opposite in each layer. Moreover, this is accompanied by vertical shear in the velocity fields (not shown in the figure). Hence, we interpret this Hopf bifurcation as a mixed barotropic/baroclinic instability. The same plot for the Hopf bifurcation H_2 is given in Figure 13. Here, we see again that positive and negative anomalies are opposite in each layer. Therefore, we interpret this Hopf bifurcation also as a mixed barotropic/baroclinic instability.

The periodic orbits. The physical patterns associated with periodic dynamics change with the parameters U_0 and h_0. Namely the propagation features of the periodic orbits in Figures 3 and 4 differ from those at the Hopf bifurcations that gave birth to these orbits. The vorticity field associated with the periodic orbit in Figure 3 propagates eastward in the bottom layer, whereas it does not propagate in the top layer, see the Hovmöller diagram in Figure 14. Also, the variability is stronger in the top layer. The vorticity field associated with the periodic orbit in Figure 4 is non-propagating in both layers (Figure 15).

Period doublings. The strange attractor after the period doubling sequence is associated with non-propagating wave behaviour in both layers (Figure 16). The characteristic time scale is approximately 100 days. Again the variability is stronger in the upper layer.

Broken torus. The dynamics on the broken 2-torus attractor corresponds to non-propagating wave behaviour in both layers (Figure 17). The dominant time scale in the top layer (approximately 50 days) is longer than in the bottom layer (5 to 10 days). Both time scales are represented by peaks in the power spectrum (Figure 8).

Intermittency. The strange attractor in Figure 10 is characterised by intermittent transitions between long time episodes of nearly stationary behaviour and episodes with eastward propagating waves in the bottom layer and non-propagating waves in the top layer, see Figure 18.

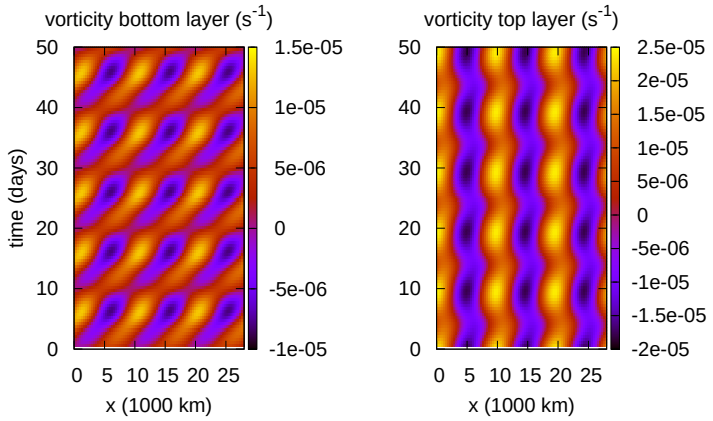

Figure 14: Hovmöller diagram of the periodic orbit of Figure 3. The magnitude of the vorticity field is plotted as a function of time and longitude while keeping the latitude fixed at $y = 1250$ km. Observe the eastward propagation in the bottom layer.

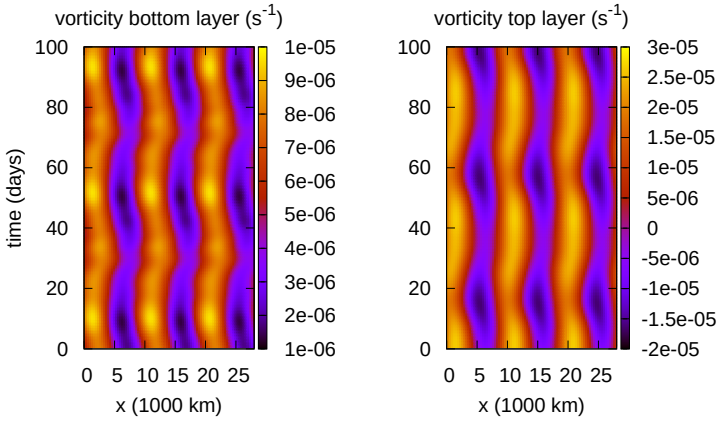

Figure 15: Same as Figure 14 for the periodic orbit of Figure 4. Observe that this wave is non-propagating in both layers.

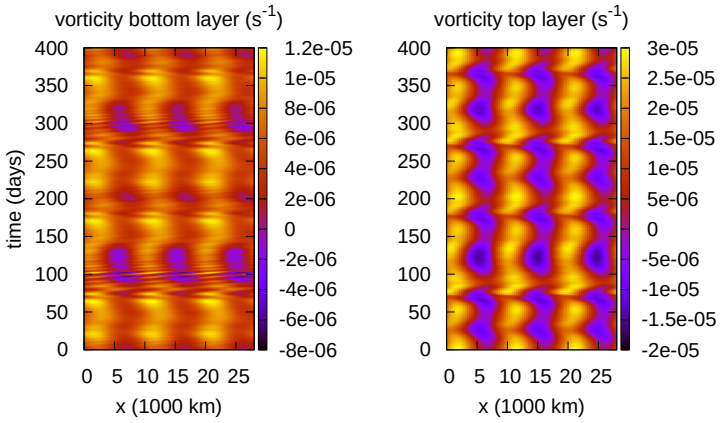

Figure 16: Same as Figure 14 for the strange attractor of Figure 7. The non-propagating nature is inherited from the periodic orbit of Figure 3. Observe the irregular variability in the bottom layer. This is due to the harmonics induced by the period doubling bifurcations.

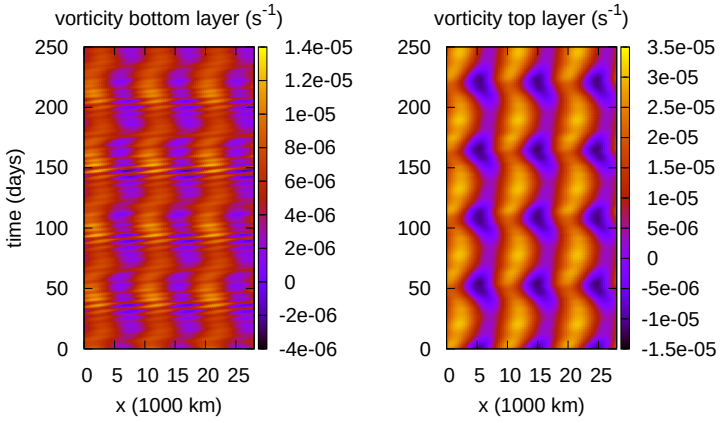

Figure 17: Same as Figure 14 for the strange attractor of Figure 8. Again, the non-propagating nature is inherited from the periodic orbit of Figure 3. The two fundamental frequencies (11 and 56 days) of the formerly existing 2-torus can still be identified.

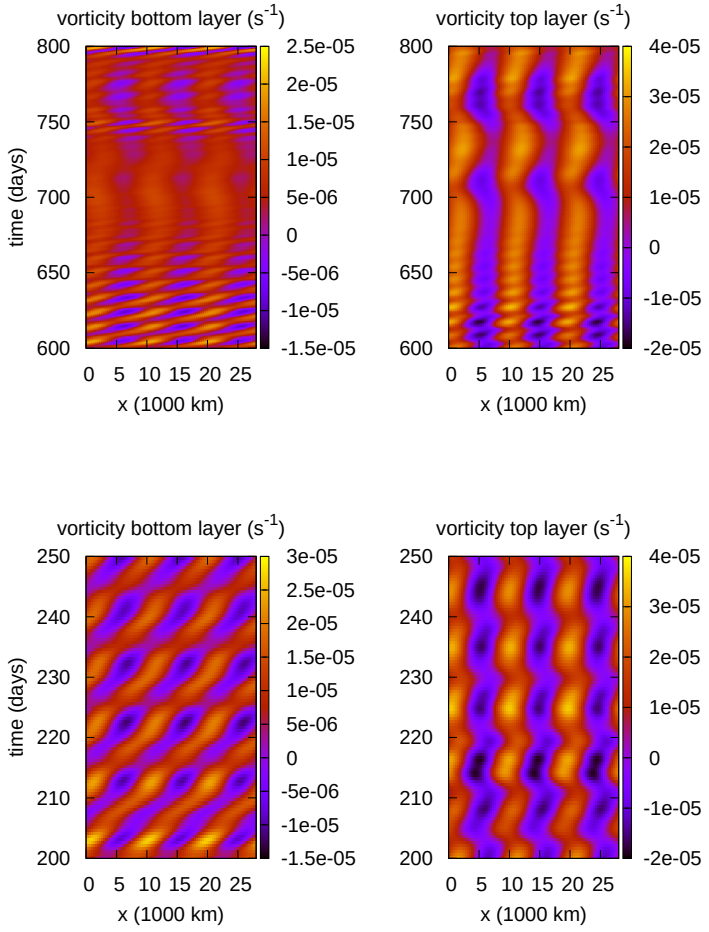

Figure 18: Hovmöller diagrams of the strange attractor of Figure 10 for two different time intervals. The magnitude of the vorticity field is plotted as a function of time and longitude while keeping the latitude fixed at $y = 1250$ km. The lower panels correspond to the intermittency regime near the vanished periodic orbit. The propagating nature in the bottom layer is inherited from the periodic orbit of Figure 4. The top panels are associated with a stationary regime, where the orbit approaches one of the nearby equilibria.

4. Summary and discussion

In this paper we investigated the dynamical mechanisms underlying the phenomenon of low-frequency atmospheric behaviour. Our results indicate that the basic process consists of planetary scale mixed baroclinic/barotropic instabilities. A fundamental role is played by the interaction of the westerly flow with orography at zonal wavenumber three. Characteristic timescales are in the range 10-200 days, where the lower frequency components (60-200 days) can be interpreted as harmonics of dominant frequencies in the range 10-60 days. The above features largely agree with previous studies based on observations and orographic resonance theories [5, 6, 33, 34].

We considered a low-order model derived from the 2-layer shallow water equations. Low-frequency behaviour is exhibited by the model for physically meaningful parameter values. Here the model dynamics is chaotic, taking place on a strange attractor, and is associated with irregularly recurring flow patterns. The dominant time scales and the spatial patterns are inherited from two branches of periodic orbits that gave birth to the strange attractor through various bifurcation scenarios. This intermittent behaviour is found in a relatively large domain of physically relevant parameter values.

The dynamics of the low-order model is analysed and interpreted using techniques from the theory of dynamical systems. A bifurcation study is carried out using orography height and magnitude of zonal wind forcing as control parameters. Many codimension two bifurcations of equilibria and periodic orbits act as organising centres of the parameter plane. A stable equilibrium exists for small U_0. Stable periodic orbits appear for U_0 larger than 12.5 m/s due to Hopf bifurcations, and they are persistent in a large domain of the parameter plane. Strange attractors occur in the region near $U_0 \geq 14.5$ m/s and $h_0 \geq 850$ m, and are created from the periodic orbits through various scenarios: period doubling cascades, Hopf-Neĭmark-Sacker bifurcations followed by breakdown of a 2-torus attractor, and saddle-node bifurcations taking place on strange attractors.

Comparison with the literature. The temporal and spatial scales identified in our study agree with the observational evidence (see e.g. [6, 30, 33]), indicating that low-frequency variability in the Northern Hemisphere is concentrated in the spectral region corresponding to periods of 10 days or larger and zonal wavenumbers less than 5.

However, the dynamical mechanisms identified in our work (see above) are novel. Many studies invoke the 'multiple-equilibria theory' of Charney

and DeVore [18] and are based on barotropic models. The dynamics typically involves a Shil′nikov homoclinic bifurcation near a Hopf-saddle-node bifurcation of an equilibrium, see [15] for an overview. Crommelin et al. [22] propose the multiple equilibrium approach in the presence of a Shil′nikov homoclinic bifurcation. Low-frequency variability is explained in terms of intermittent transitions between two preferred flow patterns. However, this requires parameters to be near both a Shil′nikov bifurcation and a saddle-node bifurcation of equilibria. This restricts the validity to a neighbourhood of an isolated point in a 2-dimensional parameter plane. In our model, low-frequency variability arises from periodic orbits bifurcating into strange attractors. This is accomplished via different routes and persists in a large parameter domain. From the physical viewpoint, our model does not suffer from the limitations of barotropic models, the most serious one being that the source of energy of the instabilities is the kinetic rather than the available potential energy. We believe that this is the main point of advantage of our approach, which has allowed us to capture the mixed barotropic/baroclinic character of the phenomenon. In addition, by deriving the low-order model from the shallow water equations, these instabilities occur at the correct parameter values.

Open physical questions. The Hopf bifurcations have been interpreted in terms of hydrodynamic instabilities by examining the physical patterns obtained from the eigenvectors at the bifurcation. A more complete physical interpretation would also involve an analysis of the energy cycle along the lines of [41].

The periodic orbits inherit their physical patterns from the Hopf bifurcations at which they are born. However, the physical patterns associated with the periodic orbits will change with the parameters, further away from the Hopf bifurcations. Studying these changes in a systematic way is an interesting subject for future research.

Open mathematical questions. Reduction of infinite-dimensional systems to finite-dimensional systems is a challenging problem. On the one hand there are computational procedures such as discretisation by means of finite-differences or Galerkin-like projections. On the other hand there exist conceptual reductions to lower-dimensional models such as restrictions to invariant manifolds containing attractors. However, often the available theorems are not constructive. The challenge lies in reconciling the computational methods with the conceptual methods. The study presented in this paper is a first step

in the coherent analysis of the (infinite-dimensional) shallow water model. There are two important open questions.

1. Which dynamical features of the low-order model persist as the number of retained Fourier modes is increased in the Galerkin projection?
2. Which dynamical features of the low-order model persist in the infinite-dimensional shallow water model?

For the first, one can think of the approach used in [52, 53, 54] for a Rayleigh-Bénard convection problem. A strongly related issue is the investigation of models with an increasing number of layers in the vertical direction.

A rigorous mathematical investigation of the infinite-dimensional system should be undertaken together with computational work. For example, what is the state space of the infinite-dimensional model generated by the equations (5)? Answering this question requires proving the existence of (weak) solutions. The idea would be to follow the methods used for the 2-dimensional Navier-Stokes equations and certain reaction-diffusion equations, see [57, 62]. For these equations the Galerkin method is used to construct a sequence of successive approximations which converge to a solution of the weak form of the equations in a suitable Hilbert space. This Hilbert space then serves as a suitable state space on which an evolution operator can be defined. When this has been achieved one can try to prove the existence of finite-dimensional global attractors or inertial manifolds.

Acknowledgements

AES is financially supported by the Netherlands Organisation for Scientific Research (NWO) by grant ALW 854.00.036. RV gratefully acknowledges support of the Willis Research Network (www.willisresearchnetwork.com). The University of Barcelona is kindly thanked for its hospitality. The research of CS has been supported by grant MTM2006-05849/Consolider (Spain).

A. Numerical methods

The numerical investigation of the low-order model consists of a mixture of different techniques, which are described briefly in this section. For continuation we have mainly used the program AUTO–07p [24], and most of the technology behind this software is described in [39]. For the numerical integration and the computation of Lyapunov exponents we have written tailored software and the algorithms are sketched below.

A.1. Numerical integration

The low-order model can be written symbolically as

$$\frac{dx_i}{dt} = C_i + \sum_{j=1}^{d} L_{ij} x_j + \sum_{j,k=1}^{d} Q_{ijk} x_j x_k, \quad i = 1, \ldots, d. \tag{8}$$

This system is integrated numerically by computing a truncated Taylor expansion of the solution around time t_0:

$$x_i(t_0 + h) = \sum_{n=0}^{N} x_i^{[n]}(t_0) h^n + O(h^{N+1}),$$

where the coefficients are given by

$$x_i^{[n]}(t_0) := \frac{1}{n!} \left. \frac{d^n x_i}{dt^n} \right|_{t=t_0}. \tag{9}$$

Given a point $x_i^{[0]}(t_0)$, which is either an initial condition or a previously computed point on the trajectory, we first compute

$$x_i^{[1]} = C_i + \sum_{j=1}^{d} L_{ij} x_j^{[0]} + \sum_{j,k=1}^{d} Q_{ijk} x_j^{[0]} x_k^{[0]}.$$

Then, for $n > 0$, we have the recurrent relation

$$x_i^{[n+1]} = \frac{1}{n+1} \left(\sum_{j=1}^{d} L_{ij} x_j^{[n]} + \sum_{j,k=1}^{d} \sum_{m=0}^{n} Q_{ijk} x_j^{[m]} x_k^{[n-m]} \right),$$

which follows by substituting the truncated Taylor series in (8) using the Leibniz rule for differentiation of products.

We have chosen a tolerance $\epsilon = 10^{-16}$. This gives $N = 20$ as the optimal order. The step size is then computed as $h_m = \min\{s_{m,1}, s_{m,2}\}$, where

$$s_{m,1} = \exp\left\{ \frac{1}{N-1} \log\left(\epsilon \frac{\|x^{[1]}\|_\infty}{\|x^{[N]}\|_\infty} \right) \right\},$$
$$s_{m,2} = \exp\left\{ \frac{1}{N-2} \log\left(e^2 \epsilon \frac{\|x^{[1]}\|_\infty}{\|x^{[N-1]}\|_\infty} \right) \right\}.$$

A very convenient aspect of the Taylor integration method is the possibility of producing dense output. By choosing step sizes smaller than the one given above, one can compute points along the orbits for any value of t.

For a more detailed account on the Taylor method, see [38].

A.2. Computation of Lyapunov exponents

We compute Lyapunov exponents by means of the algorithm described in [3, 4]. To compute the first k Lyapunov exponents we choose at random a set of k orthonormal vectors $v_{1,0}, \ldots, v_{k,0}$. Then we simultaneously integrate the vector field and the first variational equations:

$$\begin{aligned} \frac{dx}{dt} &= f(x), \\ \frac{dv_i}{dt} &= D_x f(x(t)) v_i, \quad i = 1, \ldots, k. \end{aligned}$$

Starting from the initial condition, we integrate the extended system for T units of time. This gives the vectors $x(T)$ and $v_i(T)$. During the integration the vectors $v_i(t)$ tend to align themselves along the direction of maximal expansion. To prevent the vectors v_i from collapsing onto one direction, a Gram-Schmidt procedure is applied to the vectors $v_1(T), \ldots, v_k(T)$, which results in a set of orthogonal vectors $\widetilde{v}_1(T), \ldots, \widetilde{v}_k(T)$. Then we replace the vectors $v_i(T)$ by the normalised vectors $\widetilde{v}_i(T) / \|\widetilde{v}_i(T)\|$. Next, we integrate again for T units of time using $x(T)$ and the normalised vectors as initial conditions. Repeating this procedure N times results in the following estimates for the Lyapunov exponents:

$$\lambda_i = \frac{1}{NT} \sum_{n=1}^{N} \log \left(\|\widetilde{v}_i(nT)\| \right), \quad i = 1, \ldots, k. \tag{10}$$

For different methods to compute Lyapunov exponents, see [26, 27].

A.3. Visualisation of attractors

The attractors of the low-order model live in a 46-dimensional space, and they have to be projected on a 2-dimensional subspace for visualisation: we use here the directions of maximal amplitude along the orbits (unless otherwise specified). These directions are computed by integrating the variational equations along the trajectory [59].

A.4. Computation of power spectra

By integrating the vector field we obtain a time series $(c_k)_{k=0}^{N-1}$ by measuring the L^2-norm of the solution at regular time intervals. In the power spectra in this paper the solutions have been sampled at time steps of $1/2$.

From this time series we compute a discrete Fourier transform (DFT) by

$$\widehat{c}_k = \frac{1}{N} \sum_{n=0}^{N-1} c_n \exp\left(-2\pi i \frac{nk}{N}\right). \tag{11}$$

The power spectrum is a plot of $|\widehat{c}_k|^2$ against the Fourier frequency $f_k = k/N$.

Before computing a power spectrum is computed, the mean is subtracted from the time series:

$$u_k = c_k - \frac{1}{N} \sum_{n=0}^{N-1} c_n.$$

Moreover, a Hamming window is applied to reduce leakage of frequencies. Define the array $(H_k)_{k=0}^{N-1}$ by

$$H_k = 0.54 - 0.46 \cos\left(\frac{2\pi k}{N}\right),$$

and set $v_k = H_k u_k$. The DFT is computed from the array $(v_k)_{k=0}^{N-1}$, and the resulting array $(\widehat{v}_k)_{k=0}^{N-1}$ is normalised by dividing by the norm of the array $(H_k)_{k=0}^{N-1}$.

All frequencies are computed modulo 1. Due to the discrete sampling procedure, all other frequencies are shifted within the interval $[0, 1)$, a phenomenon referred to as aliasing. Moreover, since our time series is real-valued, its DFT is symmetric around the frequency $f = 1/2$. Indeed, from (11) it follows that $\widehat{c}_{N-k} = \widehat{c}_k^*$.

The DFT is computed by means of a fast Fourier transform implemented in the FFTW library [31].

B. Coefficients of the low-order model

In the Galerkin projection the fields u_ℓ, v_ℓ, and h_ℓ are replaced by the truncated Fourier expansions. The resulting equations are multiplied with the basis functions and integrated over the spatial domain. This gives a set of ordinary differential equations for the time-dependent expansion coefficients.

The coefficients in the equations for the low-order model are given by integrals of (products of) the basis functions, which are readily implemented in an algebraic manipulation program. We only present formulas for the projection of terms in the equation for $\widehat{u}_\ell$ onto the basis function $c_{2m}(x; a)c_n(y; b)$. The projection of other terms are given by similar formulas. In the formulas that follow, all integrations are over the rectangle $\Omega = [0, a] \times [0, b]$.

Constant terms. These terms consist of the forcing and topography. Projection of the forcing term gives

$$\iint u_\ell^*(x,y)c_{2m}(x;a)c_n(y;b)dxdy.$$

Projection of the topography term gives

$$\iint h_b(x,y)c_{2m}(x;a)c_n(y;b)dxdy.$$

Linear terms. The linear terms are due to the pressure gradient, Coriolis force terms, dissipation, and damping terms. Projection of the term

$$\frac{\rho_1}{\rho_0}F\frac{\partial h_1}{\partial x}$$

gives

$$\begin{aligned}\frac{\rho_1}{\rho_0}F\sum\widehat{h}^c_{1,p,q}\iint c'_{2p}(x;a)c_q(y;b)c_{2m}(x;a)c_n(y;b)dxdy\\ +\widehat{h}^s_{1,p,q}\iint s'_{2p}(x;a)c_q(y;b)c_{2m}(x;a)c_n(y;b)dxdy.\end{aligned}$$

Projection of Coriolis term

$$(Ro^{-1}+\beta y)v_\ell$$

gives the terms

$$\begin{aligned}\sum Ro^{-1}\widehat{v}^c_{\ell,p,q}\iint_\Omega c_{2p}(x;a)s_q(y;b)c_{2m}(x;a)c_n(y;a)dxdy\\ +\beta\widehat{v}^c_{\ell,p,q}\iint_\Omega c_{2p}(x;a)s_q(y;b)c_{2m}(x;a)c_n(y;a)ydxdy\\ +Ro^{-1}\widehat{v}^s_{\ell,p,q}\iint_\Omega s_{2p}(x;a)s_q(y;b)c_{2m}(x;a)c_n(y;a)dxdy\\ +\beta\widehat{v}^s_{\ell,p,q}\iint_\Omega s_{2p}(x;a)s_q(y;b)c_{2m}(x;a)c_n(y;a)ydxdy.\end{aligned}$$

Projection of the Laplace diffusion term

$$Ro^{-1}E_H\Delta u_\ell$$

gives

$$Ro^{-1}E_H \sum \widehat{u}^c_{\ell,p,q} \iint [c''_{2p}(x;a)c_q(y;b) + c_{2p}(x;a)c''_q(y;b)]c_{2m}(x;a)c_n(y;b)dxdy$$
$$\widehat{u}^s_{\ell,p,q} \iint [s''_{2p}(x;a)c_q(y;b) + s_{2p}(x;a)c''_q(y;b)]c_{2m}(x;a)c_n(y;b)dxdy$$

Finally, projection of the damping term

$$-\sigma(\mu + \delta_{\ell,2}r)u_\ell$$

gives

$$-\sigma(\mu + \delta_{\ell,2}r) \sum \widehat{u}^c_{\ell,p,q}\widehat{u}^c_{\ell,m,n} \iint c_2 p(x;a)c_q(y;b)c_{2m}(x;a)c_n(y;b)dxdy$$
$$+ \widehat{u}^c_{\ell,p,q}\widehat{u}^s_{\ell,m,n} \iint s_2 p(x;a)c_q(y;b)c_{2m}(x;a)c_n(y;b)dxdy$$

Quadratic terms. The nonlinear terms in the low-order model are due to the nonlinear advection operator in the original governing equations. For example, the projection of the term

$$u_\ell \frac{\partial u_\ell}{\partial x}$$

gives the following terms in the low-order model:

$$\sum \widehat{u}^c_{\ell,p,q}\widehat{u}^c_{\ell,r,s} \iint c_{2p}(x;a)c_q(y;b)c'_{2r}(x;a)c_s(y;b)_{2m}(x;a)c_n(y;b)dxdy$$
$$+ \widehat{u}^c_{\ell,p,q}\widehat{u}^s_{\ell,r,s} \iint c_{2p}(x;a)c_q(y;b)s'_{2r}(x;a)c_s(y;b)_{2m}(x;a)c_n(y;b)dxdy$$
$$+ \widehat{u}^s_{\ell,p,q}\widehat{u}^c_{\ell,r,s} \iint s_{2p}(x;a)c_q(y;b)c'_{2r}(x;a)c_s(y;b)_{2m}(x;a)c_n(y;b)dxdy$$
$$+ \widehat{u}^s_{\ell,p,q}\widehat{u}^s_{\ell,r,s} \iint s_{2p}(x;a)c_q(y;b)s'_{2r}(x;a)c_s(y;b)_{2m}(x;a)c_n(y;b)dxdy,$$

where the summation runs over all pairs $(p,q),(r,s) \in R$.

References

[1] P.R. Bannon: Quasi-geostrophic frontogenesis over topography. *J. Atmos. Sci* **40(9)** (1983), 2266–2277.

[2] F. Baur: Extended range weather forecasting, in *Compendium of Meteorology*, Amer. Meteor. Soc., Boston, Massachussets (1951), 814–833.

[3] G. Benettin, L. Galgani, A. Giorgilli, and J.-M. Strelcyn: Lyapunov characteristic exponents for smooth dynamical systems and for Hamiltonian systems: a method for computing all of them. Part 1: theory. *Meccanica* **15** (1980) 9 – 20.

[4] G. Benettin, L. Galgani, A. Giorgilli, and J.-M. Strelcyn: Lyapunov characteristic exponents for smooth dynamical systems and for Hamiltonian systems: a method for computing all of them. Part 2: numerical application. *Meccanica* **15** (1980) 21 – 30.

[5] R. Benzi, P. Malguzzi, A. Speranza, and A. Sutera: The statistical properties of general atmospheric circulation: observational evidence and a minimal theory of bimodality. *Quart. J. Roy. Met. Soc.* **112** (1986), 661–674.

[6] R. Benzi and A. Speranza: Statistical properties of low frequency variability in the Northern Hemisphere. *J. Climate* **2** (1989), 367–379.

[7] H.W. Broer, G.B. Huitema, and M.B. Sevryuk: *Quasi-periodic Motions in Families of Dynamical Systems*, Springer LNM **1645** (1996).

[8] H.W. Broer, G.B. Huitema, F. Takens, and B.L.J. Braaksma: *Unfoldings and Bifurcations of Quasi-periodic Tori*, Memoirs of the AMS **83** (1990).

[9] H.W. Broer, R. Roussarie, and C. Simó: *On the Bogdanov-Takens bifurcation for planar diffeomorphisms.* Proc. Equadiff 91 (eds. C. Perelló, C. Simó, J. Solà-Morales) (1993), 81 – 92.

[10] H.W. Broer, C. Simó, and J.C. Tatjer: Towards global models near homoclinic tangencies of dissipative diffeomorphisms. *Nonlinearity* **11** (1998), 667 – 770.

[11] H.W. Broer, C. Simó, and R. Vitolo: Bifurcations and strange attractors in the Lorenz-84 climate model with seasonal forcing. *Nonlinearity* **15(4)** (2002), 1205 – 1267.

[12] H.W. Broer, C. Simó, and R. Vitolo: The Hopf-Saddle-Node bifurcation for fixed points of 3D-diffeomorphisms: analysis of a resonance 'bubble'. *Physica D* **237(13)** (2008), 1773 – 1799.

[13] H.W. Broer, C. Simó, and R. Vitolo: The Hopf-Saddle-Node bifurcation for fixed points of 3D-diffeomorphisms: the Arnol′d resonance web. *Bull. Belgian Math. Soc. Simon Stevin* **15(5)** (2008), 769 – 787.

[14] H.W. Broer and G. Vegter: Subordinate Shil′nikov bifurcations near some singularities of vector fields having low codimension. *ETDS* **4** (1984), 509 – 525.

[15] H.W. Broer and R. Vitolo: Dynamical systems modelling of low-frequency variability in low-order atmospheric models. *DCDS B* **10** (2008), 401 – 419.

[16] H.W. Broer and F. Takens: *Dynamical Systems and Chaos*, Epsilon Uitgaven (2009). In press.

[17] J.G. Charney and A. Eliassen: A numerical method for predicting the perturbations of the midlatitude westerlies. *Tellus* **1** (1949), 38 – 54.

[18] J.G. Charney and J.G. DeVore: Multiple Flow Equilibria in the Atmosphere and Blocking. *J. Atmos. Sci.* **36** (1979), 1205 – 1216.

[19] S. Corti, F. Molteni, and T.N. Palmer: Signature of recent climate change in frequencies of natural atmospheric circulation regimes. *Nature* **398** (1999), 799 – 802.

[20] D.T. Crommelin: Homoclinic Dynamics: A Scenario for Atmospheric Ultralow-Frequency Variability. *J. Atmos. Sci.* **59(9)** (2002), 1533–1549.

[21] D.T. Crommelin: Regime transitions and heteroclinic connections in a barotropic atmosphere. *J. Atmos. Sci.* **60(2)** (2003), 229 – 246.

[22] D.T. Crommelin, J.D. Opsteegh, and F. Verhulst: A mechanism for atmospheric regime behaviour. *J. Atmos. Sci.* **61(12)** (2004), 1406 – 1419.

[23] R.L. Devaney: *An Introduction to Chaotic Dynamical Systems* (2nd edition), Addison–Wesley (1989).

[24] E.J. Doedel and B.E. Oldeman: *AUTO–07p: continuation and bifurcation software for ordinary differential equations*. Concordia University, Montreal, Canada.

[25] R.M. Dole: Persistent anomalies of the extratropical Northern Hemisphere wintertime circulation. in *Large-Scale Dynamical Processes in the Atmosphere*, B. J. Hoskins and R. P. Pearce Eds, Elsevier, New York, 1983, pp. 95 – 109.

[26] L. Dieci, R.D. Russel, and E.S. van Vleck: On the computation of Lyapunov exponents for continuous dynamical systems. *SIAM J. Num. Anal.* **34** (1997), 402 – 423.

[27] L. Dieci: Jacobian free computation of Lyapunov exponents. *J. Dyn. Diff. Eq.* **14** (2002), 697 – 717.

[28] H.A. Dijkstra: *Nonlinear Physical Oceanography* (second revised and enlarged edition), Springer (2005).

[29] H.A. Dijkstra: *Dynamical Oceanography*, Springer (2008).

[30] Klaus Fraedrich and Horst Böttger. A wavenumber-frequency analysis of the 500 mb geopotential at 50°N. *J. Atmos. Sci* **35(4)** (1978), 745–750.

[31] M. Frigo and S.G. Johnson: The Design and Implementation of FFTW3. *Proceedings of the IEEE* **93** (2005), 216 – 231.

[32] J. Guckenheimer and P. Holmes: *Nonlinear Oscillations, Dynamical Systems, and Bifurcations of Vector Fields*, Springer (1983).

[33] A.R. Hansen and A. Sutera: On the probability density distribution of planetary-scale atmospheric wave amplitude. *J. Atmos. Sci.* **43** (1986), 3250 – 3265.

[34] A.R. Hansen and A. Sutera, 1995: The probability density distribution of planetary-scale atmospheric wave amplitude revisited. *J. Atmos. Sci.* **52** (1995), 2463 – 2472.

[35] E. Hovmöller: The trough and ridge diagram. *Tellus* **1** (1949), 62 – 66.

[36] J.R. Holton: *An Introduction to Dynamic Meteorology*, fourth edition, Academic Press (2004).

[37] H. Itoh and M. Kimoto: Multiple attractors and chaotic itinerancy in a quasigeostrophic model with realistic topography: Implications for weather regimes and low-frequency variability. *J. Atmos. Sci.* **53** (1996), 2217 – 2231.

[38] À. Jorba and M. Zou: A software package for the numerical integration of ODEs by means of high-order Taylor methods. *Experimental Mathematics* **14** (2005), 99 – 117.

[39] Yu.A. Kuznetsov: *Elements of Applied Bifurcation Theory*, third edition, Springer (2004).

[40] B. Legras and M. Ghil: Persistent anomalies, blocking and variations in atmospheric predictability. *J. Atm. Sci.* **42** (1985), 433 – 471.

[41] E.N. Lorenz: *The nature and theory of the general circulation of the atmosphere.* World Meteorological Organization, No. 218, TP 115 (1967), 161 pp. Available at `http://eapsweb.mit.edu/research/Lorenz/publications.htm`

[42] E.N. Lorenz: Attractor Sets and Quasi-Geostrophic Equilibrium. *J. Atm. Sci.* **37**, (1980) 1685 – 1699.

[43] V. Lucarini, A. Speranza, and R. Vitolo: Parametric smoothness and self-scaling of the statistical properties of a minimal climate model: What beyond the mean field theories? *Physica D* **234(2)** (2007), 105 – 123.

[44] P. Malguzzi and A. Speranza: Local Multiple Equilibria and Regional Atmospheric Blocking. *J. Atmos. Sci.* **38** (1981), 1939 – 1948.

[45] P. Malguzzi, A. Speranza, A. Sutera, and R. Caballero: Nonlinear amplification of stationary Rossby waves near resonance, Part I. *J. Atmos. Sci.* **53** (1996), 298 – 311.

[46] P. Malguzzi, A. Speranza, A. Sutera, and R. Caballero: Nonlinear amplification of stationary Rossby waves near resonance, Part II. *J. Atmos. Sci.* **54** (1997), 2441 – 2451.

[47] K. Mo and M. Ghil: Cluster analysis of multiple planetary flow regimes. *J. Geophys. Res.* **93** (1988), 10927 – 10952.

[48] G. Nitsche, J.M. Wallace and C. Kooperberg: Is there evidence of multiple equilibria in planetary wave amplitude statistics? *J. Atmos. Sci.* **51** (1994), 314 – 322.

[49] J. Palis and F. Takens: *Hyperbolicity and Sensitive Chaotic Dynamics at Homoclinic Bifurcations*, Cambridge University Press (1993).

[50] T.N. Palmer, F.J. Doblas-Reyes, A. Weisheimer, and M.J. Rodwell: Toward seamless prediction: Calibration of climate change projections using seasonal forecasts. *Bull. Am. Met. Soc.* **89(4)** (2008), 459 – 470.

[51] Y. Pomeau and P. Manneville: Intermittent transition to turbulence in dissipative dynamical systems. *Comm. Math. Phys.* **74** (1980), 189 – 197.

[52] D. Puigjaner, J. Herrero, F. Giralt, and C. Simó: Stability analysis of the flow in a cubical cavity heated from below. *Physics of Fluids* **16** (2004), 3639 – 3655.

[53] D. Puigjaner, J. Herrero, F. Giralt, and C. Simó: Bifurcation analysis of multiple steady flow patterns for Rayleigh-Bénard convection in a cubical cavity at $Pr = 130$. *Physical Review E* **73** (2006), 046304.

[54] D. Puigjaner, J. Herrero, C. Simó, and F. Giralt: Bifurcation analysis of steady Rayleigh–Bénard convection in a cubical cavity with conducting sidewalls. *J. Fluid Mechanics* **598** (2008), 393 – 427.

[55] B. Reinhold: Weather Regimes – The Challenge in Extended-Range Forecasting. *Science* **235(4787)** (1987), 437–441.

[56] D.F. Rex: Blocking action in the middle troposphere and its effect upon regional climate. Part 2: The climatology of blocking action. *Tellus* **2** (1950), 275 – 301.

[57] J.C. Robinson: *Infinite-dimensional dynamical systems*, Cambridge University Press (2001).

[58] P.M. Ruti, V. Lucarini, A. dell'Aquila, S. Calmanti, and A. Speranza: Does the subtropical jet catalyze the midlatitude atmospheric regimes? *Geophys. Res. Lett.* **33** L06814 (2006), 4 pp.

[59] C. Simó: On the analytical and numerical computation of invariant manifolds, in *Modern Methods of Celestial Mechanics* (D. Benest and C. Froeschlé Eds.) ed. Frontières, Paris (1990), 285 – 330.

[60] D.B. Stephenson, A. Hannachi, and A. O'Neil: On the existence of multiple climate regimes. *Quart. J. Roy. Met. Soc.* **130** (2004), 583 – 605.

[61] H.E. de Swart: Analysis of a six-component atmospheric spectral model: chaos, predictability and vacillation. *Physica D* **36** (1989) 222 – 234.

[62] R. Temam: *Infinite-dimensional dynamical systems in mechanics and physics*, Springer (1997).

[63] L. van Veen: Baroclinic flow and the Lorenz–84 model. *Int. J. Bifur. Chaos* **13** (2003), 2117 – 2139.

[64] S. Wieczorek, B. Krauskopf, and D. Lenstra: Unnested islands of period doublings in an injected semiconductor laser. *Phys. Rev. E* **64**, 056204 (2001).